



Contents lists available at ScienceDirect

European Journal of Medicinal Chemistry

journal homepage: <http://www.elsevier.com/locate/ejmech>

Insight into the binding mode of HIF-2 agonists through molecular dynamic simulations and biological validation

Yancheng Yu¹, Quanwei Yu¹, Simeng Liu, Chenyang Wu, Xiaojin Zhang*

Jiangsu Key Laboratory of Drug Design and Optimization, and Department of Chemistry, China Pharmaceutical University, Nanjing, 211198, China

ARTICLE INFO

Article history:

Received 27 September 2020

Received in revised form

30 October 2020

Accepted 4 November 2020

Available online xxx

Keywords:

HIF-2

Agonist

Binding mode

Molecular dynamic simulations

ABSTRACT

Hypoxia-inducible factor-2 (HIF-2), a heterodimeric transcriptional protein consisting of HIF-2 α and aryl hydrocarbon receptor nuclear translocator (ARNT) subunits, has a broad transcriptional profile that plays a vital role in human oxygen metabolism. **M1001**, a HIF-2 agonist identified by high-throughput screening (HTS), is capable of altering the conformation of Tyr281 of the HIF-2 α PAS-B domain and enhancing the affinity of HIF-2 α and ARNT for transcriptional activation. **M1002**, an analog of **M1001**, shows improved efficacy than **M1001**. However, the cocrystal structure of **M1001** and HIF-2 has some defects in revealing the agonist binding mode due to the relatively low resolution, while the binding mode of **M1002** remained unexplored. To in-depth understand agonist binding profiles, herein, the molecular dynamic (MD) simulations was applied to construct a stable agonist-protein model, and a possible binding mode was proposed through the analysis of the binding free energy and hydrogen bonding of the simulation results. Nine compounds were then synthesized and evaluated to verify the proposed binding mode. Among them, compound **10** manifested improved agonistic activity and reduced toxicity compared to **M1002**. This study provides deep insight into the binding mode of such HIF-2 agonists, which would be useful for designing novel agonists for HIF-2.

© 2020 Elsevier Masson SAS. All rights reserved.

1. Introduction

The hypoxia response signaling axis acts as a critical role in promoting adaptation to hypoxia by regulating processes such as oxygen metabolism, oxygen delivery, angiogenesis, and cell survival [1–3]. Hypoxia-inducible factor-2 (HIF-2), a member of the HIF family proteins, is a heterodimeric transcription factor composed of an oxygen-dependent HIF-2 α subunit and a stably expressed aryl hydrocarbon receptor nuclear translocator (ARNT) subunit [4,5]. HIF-2 plays a vital role in the hypoxia response signaling pathway [6], which has a wide range of target genes involved in many physiological and pathological processes. The disorder of HIF-2 contributes to corresponding pathogenesis, such

as ischemia [7] and tumorigenesis [8]. The use of small-molecule modulators to regulate HIF-2 levels has been proved as an effective strategy for the treatment of HIF-2 related diseases, of which renal anemia [7] and renal cell carcinoma [9] are most studied.

Currently, there are two main types of HIF-2 small-molecule modulators, prolyl hydroxylase domain (PHD) inhibitors [10] and HIF-2 allosteric inhibitors [11]. Under normoxic conditions, the proline residues, Pro405 and Pro531, of HIF-2 α are hydroxylated by PHD enzymes and, consequently, the hydroxylated HIF-2 α is recognized for ubiquitination and proteasome degradation. PHD inhibitors stabilize HIF by inhibiting the PHD-mediated hydroxylation process and increase the expression levels of HIF downstream genes, such as erythropoietin (EPO), cytochrome *b* (Cytb), and the ferrous ion membrane transport protein divalent metal transporter 1 (DMT1), thus promoting erythropoiesis and iron metabolism and thereby alleviating renal anemia [10].

HIF-2 α allosteric inhibitors can inhibit the dimerization and transcription of HIF-2 by changing the conformation of the HIF-2 α subunit. In 2009, a buried cavity of approximately 290 Å³ was recognized inside the HIF-2 α -PASB domain (Fig. 1B) [12]. HIF-2 α allosteric inhibitors occupy the hydrophobic cavity and push the side chain of Met252 (an internal residue) to the binding surface of

Abbreviations: ARNT, aryl hydrocarbon receptor nuclear translocator; Cytb, cytochrome *b*; DMT1, divalent metal transporter 1; ESP, electrostatic potential; EPO, erythropoietin; HIF-2, hypoxia-inducible factor-2; HREs, hypoxia response elements; MD, molecular dynamics; MM-PBSA, molecular mechanics/Poisson-Boltzmann surface area; RMSD, root mean square deviation; SAR, structure-activity relationship; PHD, prolyl hydroxylase domain; PTS, protein thermal shift.

* Corresponding author.

E-mail address: zxj@cqu.edu.cn (X. Zhang).

¹ These authors contributed equally.

<https://doi.org/10.1016/j.ejmech.2020.112999>

0223-5234/© 2020 Elsevier Masson SAS. All rights reserved.

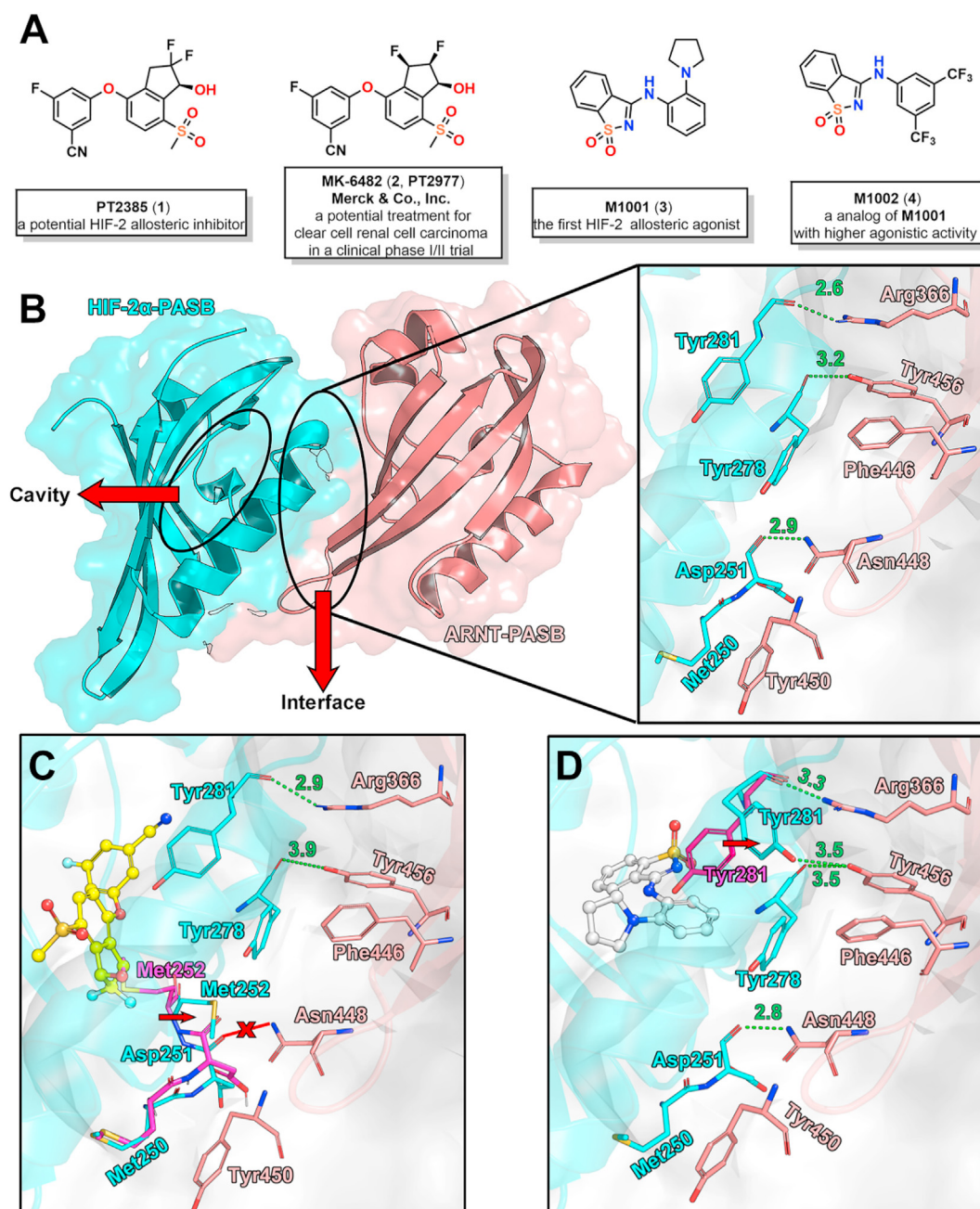


Fig. 1. (A) Representative structures of HIF-2 modulators. (B) Schematic diagram of the HIF-2-PASB domain (PDB ID:4ZP4) [17]. The cyan cartoon shows the HIF-2α-PASB domain, and the salmon cartoon shows the ARNT-PASB domain. The two oval shapes refer to the internal cavity of the HIF-2α-PASB domain and the binding interface of PASB domains of two subunits, respectively. The enlarged image on the right shows the three key hydrogen bonds (green dotted line representation) at the binding interface. (C) Schematic diagram of the mechanism of HIF-2 allosteric inhibitor (PDB ID: 6E3S) [15]. The inhibitor is represented by a yellow ball and a stick. The cyan and salmon sticks show the residues in the cocrystal structure of inhibitor **PT2385** with HIF-2 (PDB ID: 6E3S) [15]. The purple sticks show Met252, Asp251, Met250 in apo protein (PDB ID: 4ZP4) [17]. **PT2385** pushes the side chain of Met252 to the binding surface to break the hydrogen bond between Asp251 and Asn448. (D) Schematic diagram of the mechanism of the HIF-2 allosteric agonist (PDB ID: 6E3U) [15]. The agonist is represented by white ball and sticks. The cyan and salmon sticks show the residues in the cocrystal of agonist **M1001** and HIF-2 (PDB ID: 6E3U) [15]. The purple sticks show Tyr281 in apo protein (PDB ID: 4ZP4) [17]. **M1001** pushes the side chain of Tyr281 to the binding surface to form a new hydrogen bond with Tyr456. (For interpretation of the references to color in this figure legend, the reader is referred to the Web version of this article.)

HIF-2α-PAS-B and ARNT-PAS-B. Such conformational change of Met252 disrupts a critical hydrogen bond (Fig. 1C, red line representation) between Asp251 (HIF-2α-PASB domain) and Asn448 (ARNT-PASB domain), thereby impairing the dimerization and transcriptional activity of HIF-2 (Fig. 1C) [11]. The fastest-promoting HIF-2α allosteric inhibitor **PT2385** (1, Fig. 1A) [11] and **MK-6482** (2, formerly known as **PT2977**, Fig. 1A) [13] has shown promising therapeutic benefits for the treatment of advanced clear cell renal

cell carcinoma [14].

It was worth noting that in 2019, Wu et al. first identified a HIF-2α allosteric agonist **M1001** (3, Fig. 1A) based on an affinity selection-mass spectrometry (AS-MS) screening [10]. The X-ray crystal structure (PDB ID: 6E3U) of HIF-2 in complex with **M1001** has been resolved; the cocrystal structure shows that **M1001** also binds to the large internal cavity in HIF-2α-PASB [15]. **M1001** pushes the side chain of Tyr281 to the junction of the PASB domains

of the two subunits, prompting Tyr281 (HIF-2 α -PASB domain) and Tyr456 (ARNT-PASB domain) to form a hydrogen bond (Fig. 1D). Further, a structure-activity relationship (SAR) approach based on **M1001** led to a more potent analog, **M1002** (4, Fig. 1A). **M1002**, with two trifluoromethyl substituents, manifests better agonistic activity toward HIF-2 α both in the protein-based and cell-based assays. Quantitative real-time polymerase chain reaction (RT-PCR) and co-immunoprecipitation (Co-IP) assays have revealed that **M1002** can promote HIF-2 dimerization and thus exert an agonistic effect [15]. The HIF-2 α allosteric agonists could probably provide a novel strategy for the treatment of renal anemia. However, due to the relatively low resolution of the cocrystal structure of **M1001** in complex with HIF-2 α , it has some shortcomings in revealing the binding mode; for instance, the position of structural waters has not been observed in the X-ray structure [15]. Besides, the binding mode of **M1002** remains unexplored. Given that structural waters are significant in the binding pattern of HIF-2 inhibitors [11], it may also contribute to the HIF-2 agonists for the binding to HIF-2 α . However, detailed atomistic insight into the binding area is needed for designing HIF-2 agonists.

MD simulations provide a very powerful methodology in analyzing the binding of small-molecules to proteins in atomic detail. Long MD simulations can provide a detailed binding mode description and thermodynamic binding properties, such as the binding free energy. In the past few years, there had been many excellent works using MD simulations to analyze binding modes [11,12]. In 2020, research by Anderson's group utilized MD simulations to confirm that bound waters play important role in stabilizing the protein structure of the HIF-2-PASB domain [16]. In this work, MD simulations has been carried out to study the agonist-HIF-2 α -PASB complex. Our computational studies were constituted by docking studies followed by long-term all-atom MD simulations and in-depth structural and energetic analysis of the agonist in complex with a PASB domain model of HIF-2 α . The binding energy calculation, energy decomposition analysis, and hydrogen bond analysis of the simulation results provide details of the binding profile of the agonist in complex with HIF-2 α -PASB domain. Subsequently, nine compounds were synthesized and biologically evaluated for their binding affinity and agonist activity against HIF-2 using the protein thermal shift (PTS) assay and the luciferase reporter gene assay, respectively. The combination of MD simulation results and experimental data provides a clear binding pattern of the HIF-2 agonists in complex with HIF-2 α -PASB domain. We suggest a binding mode that provides a basis for the design of HIF-2 α allosteric agonists.

2. Results and discussion

2.1. MD simulation results

HIF-2 has an uncommon large hydrophobic cavity inside the PASB domain. According to the X-ray structure of HIF-2-PASB domain (PDB ID: 3F1P), there are eight structural water molecules inside the HIF2 α -PASB domain, which form a hydrogen bond network with the residues inside the cavity, including Tyr281 [12,18]. It has been suggested computationally [18] and also revealed from the X-ray structure of **M1001** with HIF-2 (PDB: 6E3U) [15] that when a small-molecule binds inside this cavity, the bound water molecules are driven out of the cavity. Consequently, the side chain of Tyr281 can move freely again. If the small-molecule can fit the side chain of Tyr281 to the HIF-2 α -PASB and ARNT- PASB binding junction, this small-molecule exhibits agonistic activity [15]. To explore the binding interactions of agonists, firstly, we conducted an MD simulation to study the agonist in complex with HIF-2 α -PASB domain interaction at the atomic level.

M1001 and **M1002** are currently the only two HIF-2 allosteric agonists, and previous studies have shown that **M1002** is significantly more potent than **M1001** [15]. Thus, **M1002** was chosen as the ligand for subsequent MD simulations in this study. The HIF-2-PASB domain (242–360) was selected for MD simulation and extracted from the X-ray crystal structure of **M1001** in complex with HIF-2 (PDB ID: 6E3U) [15]. Thus, **M1002** was docked with a grid-based molecular docking method using the CHARMM force field [19]. The **M1002**-HIF-2 α -PASB complex with the highest docking score was selected for MD simulation.

2.2. MM-PBSA calculated binding free energy of **M1002** with HIF-2

The model of the **M1002**-HIF-2 α -PASB complex generated from docking was emerged in a box of waters and the solvated ligand-protein complex was used as a starting structure for a 500 ns MD simulation employing the amber99sb force field [20]. The root mean square deviation (RMSD) of **M1002** and protein relative to the initial structure was calculated to evaluate the binding stability, respectively (Fig. 2A). As is observed in Fig. 2A, the protein complex reached equilibrium after 120 ns, and the RMSD converged to ca. 2 Å. The RMSD of **M1002** converges to 2.5 Å in about 120 ns.

Subsequently, *g_mmpbsa*, a gromacs tool for MM-PBSA calculations, was utilized to calculate the binding free energy of **M1002** and protein using the molecular mechanics/Poisson-Boltzmann surface area (MM-PBSA) method [21]. The binding free energy calculated by the MM-PBSA method includes the following four items: The van der Waals contribution, and the electrostatic energy calculated with amber99sb force field, and the non-polar contribution in free energy of solvation calculated by empirical model, and the electrostatic contribution in the free energy of solvation calculated by Poisson-Boltzmann Equation. We sampled 500 snapshots every nanosecond to calculate the binding free energy and plotted the RMSD value and binding free energy of **M1002** (Fig. 2B). As the conformation of **M1002** gradually converged, the binding free energy gradually decreased from the initial −90 kJ/mol (Fig. 2B, RMSD = 0, blue dot), which demonstrated that a more stable conformation than the initial one was finally obtained. The final 300 ns binding free energy data were extracted and averaged (Table 1). The average MM-PBSA binding free energy of **M1002** with protein is -130.47 ± 12.09 kJ/mol. The binding of **M1002** to protein is dominated by van der Waals force, which is similar to most ligand binding (Table 1).

Key protein residues for binding with **M1002.** To understand the key residues that **M1002** binds to protein binding area, the MM-PBSA binding free energy was decomposed for each protein residue-ligand interaction (Fig. 3). The results indicated that Met289 and Tyr307 are the two residues that contributed most to binding, with binding energy contributions -9.33 ± 0.12 kJ/mol and -7.92 ± 0.14 kJ/mol, respectively, followed by His248 (-6.07 ± 0.11 kJ/mol) and then Met252, Phe254, and Cys339 (Fig. 3A and Fig. 3B).

Analysis of binding interactions. To investigate how **M1002** binds to these six key residues, we first analyzed the hydrogen bonds between **M1002** and protein. The results (Table 2) show that the oxygen atom of **M1002** forms a hydrogen bond with Tyr307 for 76.47% of the 500 ns MD simulation trajectory. It is worth noting that a stable bound water molecule was observed that forms a hydrogen bond with the N1 atom of **M1002** with 50.98% frequency. Furthermore, this bound water forms a hydrogen bond with interaction frequency 115.69% with His248 and a hydrogen bond with frequency 23.53% with Cys339. This hydrogen bond network formed between **M1002**, bound water, His248, and Cys339 should stabilize considerably the binding of the ligand (See a video generated with Pymol v.2.3.0 demonstrating the hydrogen bonds in

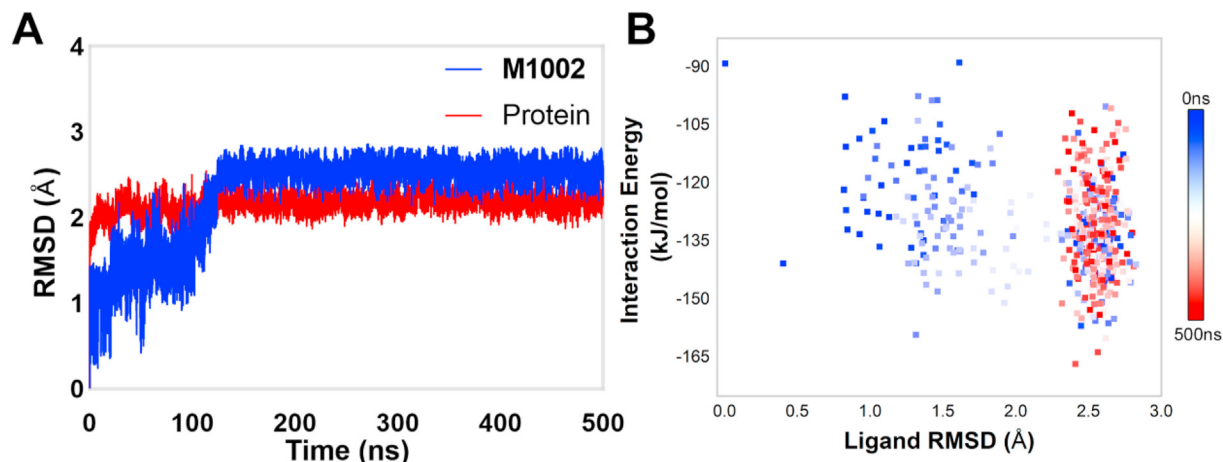


Fig. 2. (A) RMSD of **M1002** (blue) and HIF-2 α -PASB (red). (B) From 0 ns to 500 ns, the RMSD of **M1002** converges to 2.5 Å after 120 ns, and the binding energy decreases from -90 kJ/mol at the beginning of the simulations to an average of -130 kJ/mol at the end of the simulations. (For interpretation of the references to color in this figure legend, the reader is referred to the Web version of this article.)

Table 1

MM-PBSA binding energy of **M1002** to HIF-2 α -PASB.

Complex	ΔVDW^a	$\Delta Elec^b$	$\Delta Apol^c$	ΔPol^d	ΔE^e
M1002 -PASB	-214.12 ± 11.78	-51.09 ± 8.36	-17.78 ± 0.67	152.53 ± 8.18	-130.47 ± 12.09

^a ΔVDW (kJ/mol): change of van der Waals energy in the gas phase upon complex formation.

^b $\Delta Elec$ (kJ/mol): change of electrostatic interactions upon complex formation.

^c $\Delta Apol$ (kJ/mol): change of nonpolar solvation energy upon complex formation.

^d ΔPol (kJ/mol): change of polar solvation energy upon complex formation.

^e ΔE (kJ/mol): MM-PBSA binding energy.

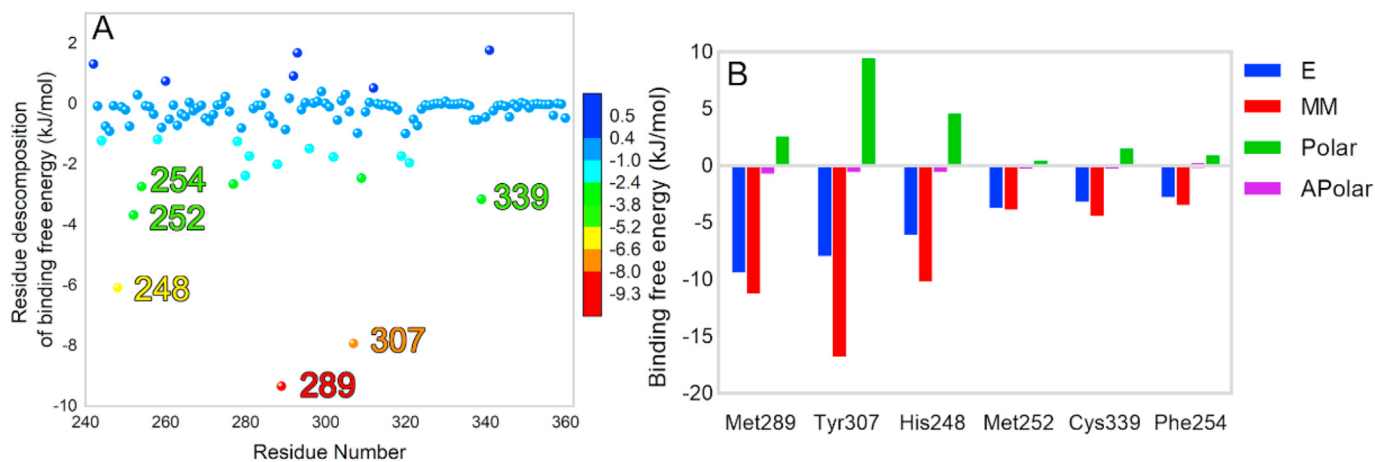
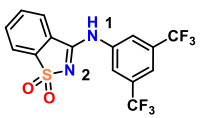


Fig. 3. (A) MM-PBSA binding free energy decomposition for the interaction of each protein residue with the ligand. (B) Histogram showing the contribution of the six residues contributing most to the binding free energy of the **M1002**-protein complex.

Table 2

Hydrogen bonds analysis of **M1002** in complex with HIF-2 α -PASB^a.

Compound	Donor	Acceptor	Occupancy
 M1002	Tyr307-OH	M1002-O2	76.47%
	M1002-N1	Water -O	50.98%
	Water-O, His248-CE1	His248-ND1, Water-O	115.69%
	Water-O	Cys339-SG	23.53%

^a Hydrogen bonds analysis angel cutoff (degrees) = 30 and donor-acceptor distance cutoff (Å) = 3.5.

Supplementary data).

Supplementary video related to this article can be found at <http://doi:10.1016/j.ejmech.2020.112999>

The snapshot in Fig. 4 shows **M1002** forming hydrogen bonds with Tyr307 and the bound water, which is consistent with the previous hydrogen bond analysis results. The side chain of Phe254 and the benzene ring of **M1002** have a π - π stacking interaction (Fig. 4) [22]. Besides, the interaction between the aromatic ring and the sulfur atom also plays a role in stabilizing the protein structure [23,24]. The benzene ring of **M1002** which is substituted by two trifluoromethyl groups may be partially positively charged, and the lone pairs on the sulfur atoms of residues Met252 and Met289 may form an $n \rightarrow \pi^*$ interaction with benzene ring [25]. Overall, we calculate that six residues participating in binding through hydrogen bonds and hydrophobic interactions.

2.3. Comparison of the binding modes of **M1001** and **M1002**

In the previous report, **M1002** has been proved to exhibit better HIF-2 binding affinity and agonist activity than **M1001** [15]. We tried to utilize the predicted binding mode of **M1002** to explain why **M1002** showed improved binding affinity than **M1001**. The co-crystal structure of **M1001** and HIF-2 (6E3U) was superimposed with the representative binding pose of **M1002** extracted from convergent trajectory (Fig. 5) using the protocol "superimpose proteins" in Discovery Studio software (version 2020).

From the results of superposition, overall, **M1002** has a binding mode similar to **M1001** (Fig. 5, left). In detail, due to the steric hindrance of Tyr278 at the edge of the cavity, the relative position of **M1002** in the cavity has changed compared to **M1001**. The trifluoromethyl group of **M1002** occupies the position of the benzene ring of **M1001**, causing the overall position of **M1002** to move upward (Fig. 5, right). As a result, the oxygen atom of the sulfone moiety of **M1002** (3.0 Å), which plays an key role in binding in our prediction, is closer to Tyr307 than that of **M1001** (4.2 Å). The close distance between the sulfone moiety and Tyr307 makes **M1002** more capable of forming hydrogen bond with Tyr307, which may be the reason why **M1002** has better affinity and agonistic activity than **M1001**. In summary, the 3,5-disubstituted benzene ring is

supposed to be the local preferential structure.

2.4. Design and synthesis of analogs of **M1002** based on the suggested binding mode

Design of the structure of the new analogs of **M1002.** Nine compounds (Fig. 6) were designed and synthesized based on the MD simulation results for validation of the suggested binding mode. Our hypothesis used for the design divides the reference structure of **M1002** into three parts: A-ring, atom linker, and B-ring (Fig. 6). Regarding the B-ring, we speculated that an electron-deficient B-ring may increase $n \rightarrow \pi^*$ interactions with the electron-rich sulfur atoms of Met289 and M252. Thus, we designed compounds **5–10** by introducing substituents having different electronic effects for investigating the interaction between the B-ring and two methionines. Regarding the atom linker, the MD simulation results suggest that it forms a hydrogen bond network through a bound water with His248 and Cys339. We methylated the NH group of **M1002** to obtain **12** for examining the effect of this possible hydrogen bond to binding. We replaced the NH moiety with an oxygen atom to **11** to investigate whether the linked moiety should present as a hydrogen bond donor. To investigate SAR for A ring, we replaced the sulfonamide with an amide moiety to **13** for exploring if this change should reduce activity through weakening hydrogen bond with Tyr307.

Synthesis of the designed analogs of **M1002.** The synthesis of the target compounds is shown in Scheme 1. Saccharin (**1a**) was selected as the raw material for the synthesis of **4–12**. **1a** was chlorinated with phosphorus pentachloride to give **2a**. Then **2a** was condensed with the corresponding amines and 3,5-bis(trifluoromethyl) phenol to give **4–11** [26]. **12** was obtained by methylation of **4** with iodomethane. **13** was synthesized through a ring-forming condensation reaction, followed by a substitution reaction [27,28].

2.5. Biological assays

Two methods were employed to evaluate the activity of the target compounds: 1. the protein thermal shift (PTS) assay [29] was

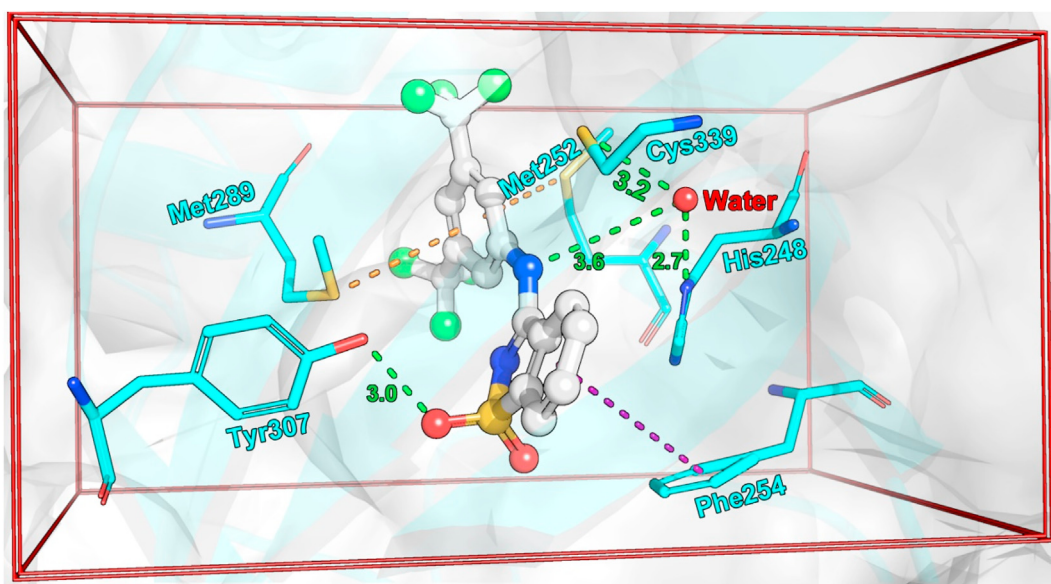


Fig. 4. Snapshot of **M1002**-protein complex from 500 ns-MD simulation using amber99sb force field. The green dotted line in the figure represents the hydrogen bond interaction, the yellow dotted line represents the $n \rightarrow \pi^*$ interaction, and the purple dotted line represents the π - π interaction. (For interpretation of the references to color in this figure legend, the reader is referred to the Web version of this article.)

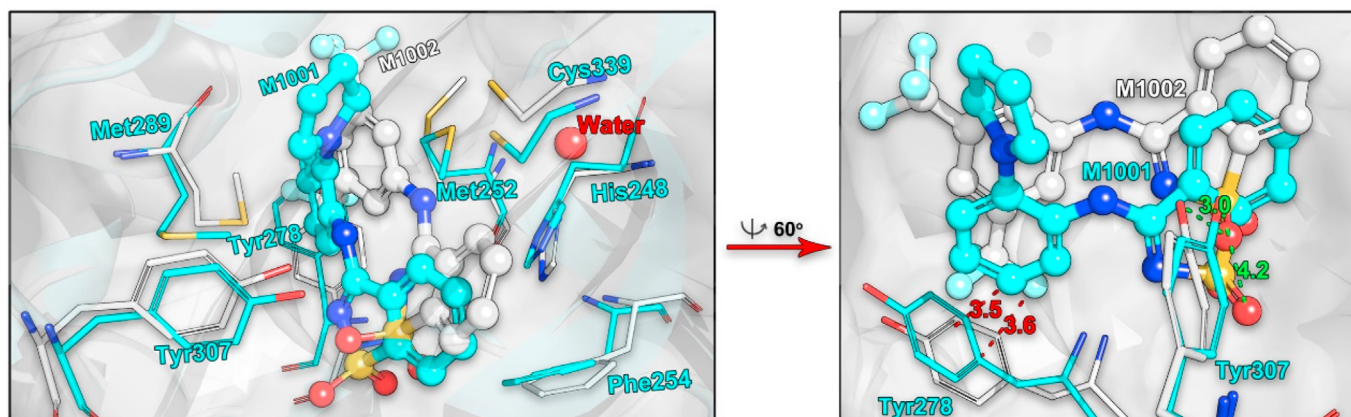


Fig. 5. Comparison of the binding modes of **M1001** and **M1002**. **M1001** is a cyan ball-and-stick representation, and its nearby residues are displayed as cyan sticks. **M1002** and the corresponding residues are grey. The two red dotted lines indicate the distance between the center of the benzene ring of Tyr278 and the trifluoromethyl group of **M1002** (3.6 Å) and the distance between the center of the benzene ring of Tyr278 and the benzene ring of **M1001** (3.5 Å), respectively. The two green dashed lines indicate the distance between the hydroxyl group of Tyr307 and the oxygen atom in the sulfone moiety of **M1002** (3.0 Å) and **M1001** (4.2 Å), respectively. (For interpretation of the references to color in this figure legend, the reader is referred to the Web version of this article.)

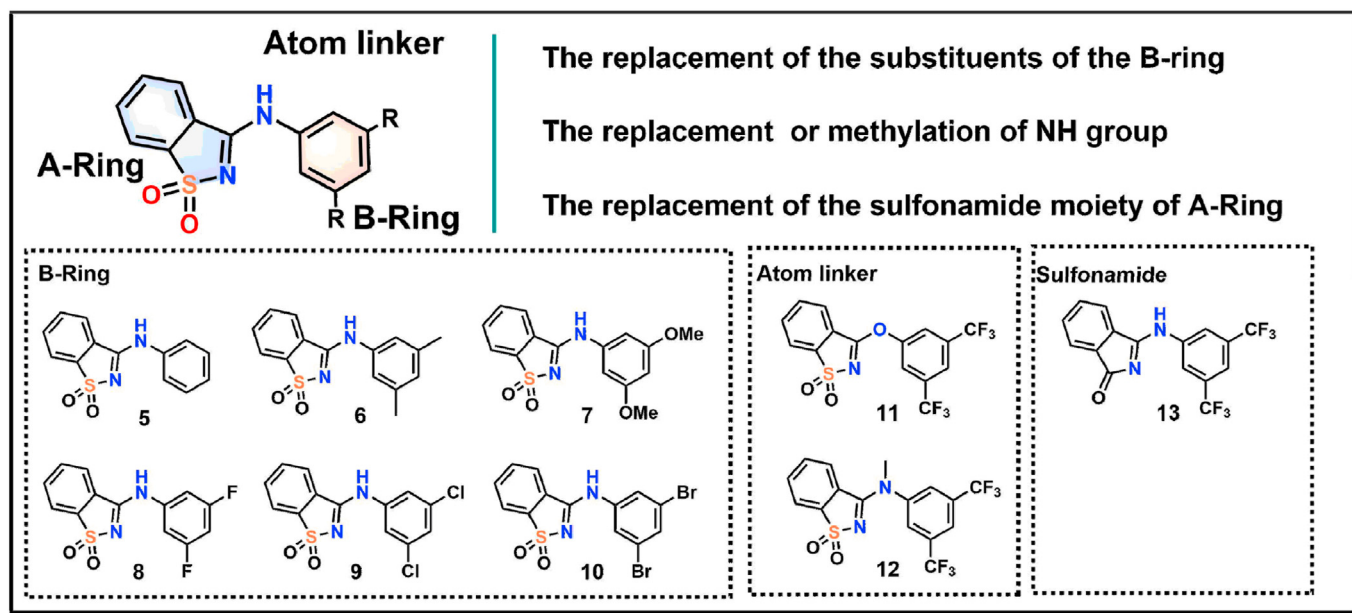


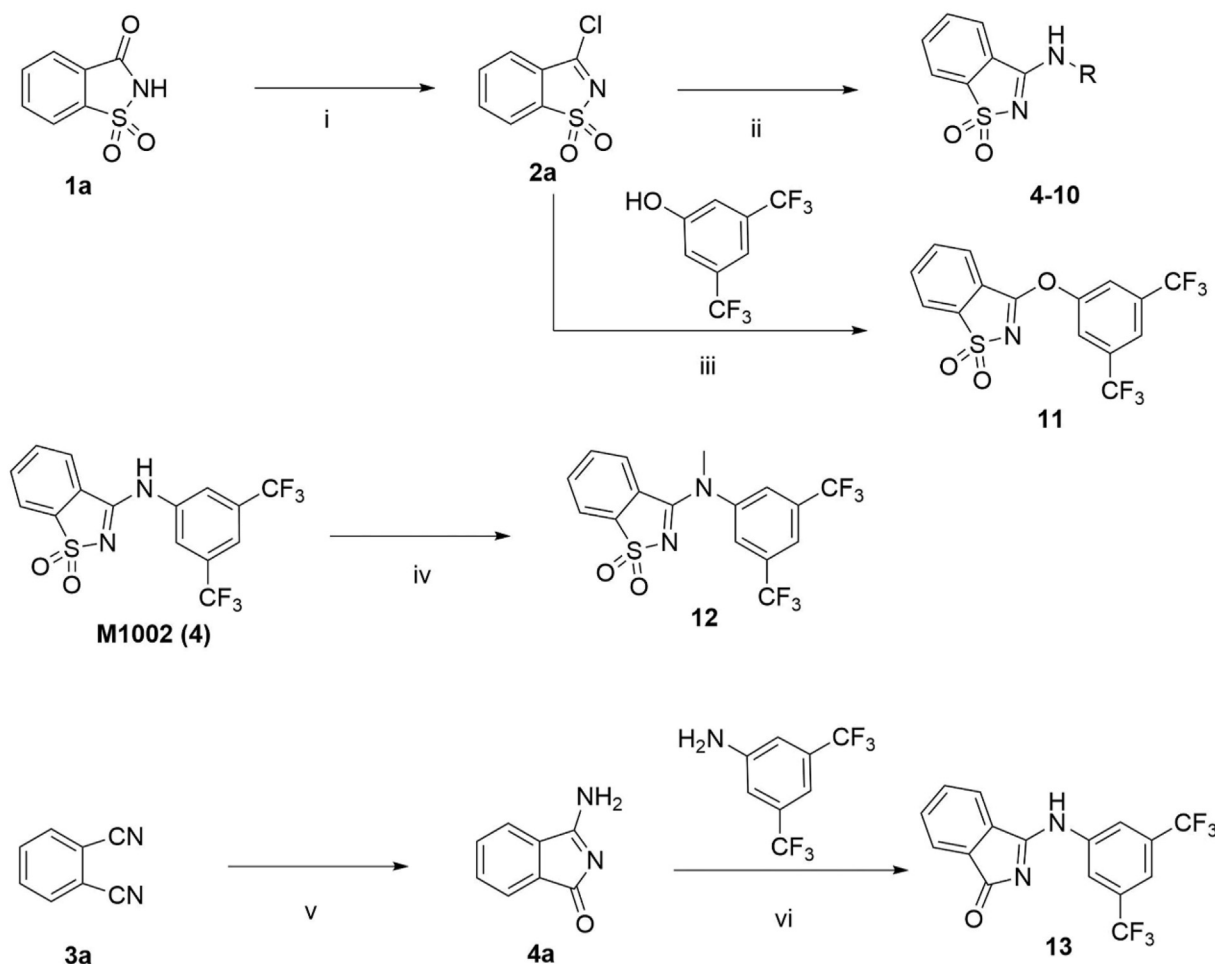
Fig. 6. Design of analogs of **M1002** as probes to explore its binding profile with protein.

selected to evaluate the binding affinity of the target compounds with HIF-2; 2. The luciferase reporter gene assay was employed to evaluate the compounds' agonistic activity on HIF-2.

Protein thermal shift assay. The PTS data of the target compounds are shown in Fig. 7. We first analyzed compounds **5–10** with various substituents on the B-ring. Compounds **6** and **7** with methyl and methoxy substituents, respectively, should have increased the electron cloud density on the B-ring; their thermal shift ($\Delta T_m = 1.93^\circ\text{C}$ for **6**, and $\Delta T_m = 1.89^\circ\text{C}$ for **7**) was slightly weaker than that of **5** ($\Delta T_m = 2.0^\circ\text{C}$) substituted by hydrogen atoms. The trifluoromethyl-substituted **M1002** and the halogen-substituted compounds **8–10** with electron-deficient B-ring, generally, are more potent than **5–7**. This result is consistent with the previous speculation that the sulfur atom on methionine is more likely to interact with the electron-deficient aromatic ring. Additionally, compound **10** ($\Delta T_m = 2.52^\circ\text{C}$) has a significant

increase in thermal shift compared to **8** ($\Delta T_m = 2.05^\circ\text{C}$) and **9** ($\Delta T_m = 2.08^\circ\text{C}$).

In an attempt to suggest an explanation for the higher binding strength of **10** compared to **8** and **9**, we docked **10** into the binding pocket of HIF-2. The best-scored docking pose was chosen as the initial pose to conduct a 50 ns MD simulation. The ligand and protein RMSD (compared with their corresponding starting poses) were calculated to estimate the binding stability (Fig. 8A). The RMSD calculations showed that during the MD simulation, the conformation of the **10**-protein complex changed very slightly and stabilized quickly (Fig. 8A). In an attempt to compare binding modes of **10** and **M1002**, the stable pose of the **10**-protein complex was extracted to align with the previous predicted **M1002**-protein structure. It was found that **10** and **M1002** have similar binding modes to protein (Fig. 8B). The simulation results also revealed that the bromine atom of **10** may have halogen bond interaction with



Scheme 1. Synthetic routes for 4–13. Reagents and conditions: (i) PCl_5 , 160 °C, 4 h, 63%; (ii) corresponding amines, pyridine, reflux, 2–5 h, 43%–85%; (iii) pyridine, reflux, 5 h, 40% (iv) iodomethane, DMF, K_2CO_3 , rt, overnight, 54% (v) *N,N*-diethylhydroxylamine, chloroform, reflux, 3 h, 55%; (vi) acetic acid, ethanol, reflux, 5 h, 34%.

the hydroxyl oxygen atom and the benzene ring of Tyr278 (Fig. 8C). The halogen bond between halogen and the benzene ring of tyrosine is the most common form of halogen bond found in PDB database statistics [30]. Statistics show that the distance of the halogen bond formed by bromine is the sum of van der Waals radii of bromine and its partner (the sum of van der Waals radii of the bromine atom and the oxygen atom is approximately 3.5 Å), and the C–Br...Donor bond angle is approximately 155° [30,31]. In our simulation results, the bromine atom of **10** can form a halogen bond with Tyr278 in most frames of simulation. The representative pose of the **10**-protein complex was extracted from the trajectory, and the distances and angles between the bromine atom and Tyr278 were measured. In the conformation we extracted, the distances of bromine from the center of the benzene ring and the oxygen atom both are 3.6 Å, and the bond angles are 164.4° and 147.7°, respectively. Additionally, we calculated the electrostatic potential (ESP) surfaces [32,33] for the docking pose between **10** and Tyr278. The results show that the positively charged region on the surface of the bromine atom can interact with the negatively charged region of Tyr278 (Fig. 8D). These geometric features and ESP surfaces indicate that a slightly positive region, known as σ -hole [34] which can be generated on the bromine atom, may indeed be capable of forming a halogen bond with Tyr278 and enhance the binding affinity of **10**. In the case of chlorine, as in **9**, the σ -hole is much less positive. For fluorine, as in **8**, no positive region is observed (the ESP

surfaces of **8**, **9**, and **10** are calculated and displayed in the supplementary data, Fig. S1). These results may provide an explanation why compound **10** in which the benzene ring is substituted with Br is stronger binder compared to **8** and **9**, with Cl or F substituents, in the PTS assay (Fig. 7).

The PTS data of **12** show that removing the hydrogen of the NH linker is detrimental for its binding to HIF-2, suggesting that the hydrogen bond network that formed by the NH linker and bound water and residues is essential for binding. As in **11**, replacing the nitrogen atom with an oxygen atom also leads to significant loss of activity, suggesting that the linker between the A and B ring should be a hydrogen bond donor in the formation of a hydrogen bond with bound water. As in **13**, replacing the sulfonamide structure with an amide also results in a significant loss of activity; it indicates that the geometry of the sulfonamide structure is indispensable in the formation of hydrogen bonds with Tyr307. Compared with the tetrahedral sulfonamide, the amide is planar and the orientation of the hydrogen bond acceptor changes, thus resulting in the inability for **13** to form hydrogen bond interactions with Tyr307 with a subsequent loss of activity.

Luciferase reporter gene assay. 786-O-HRE-Luc single clone cells were used to verify the results of the PTS assay. We evaluated the agonistic effect of **5**–**10**, and **M1002** was selected as the control compound. The 786-O-HRE-Luc cells were treated with 2 μM and 20 μM compounds, respectively, for 24 h and then tested. The

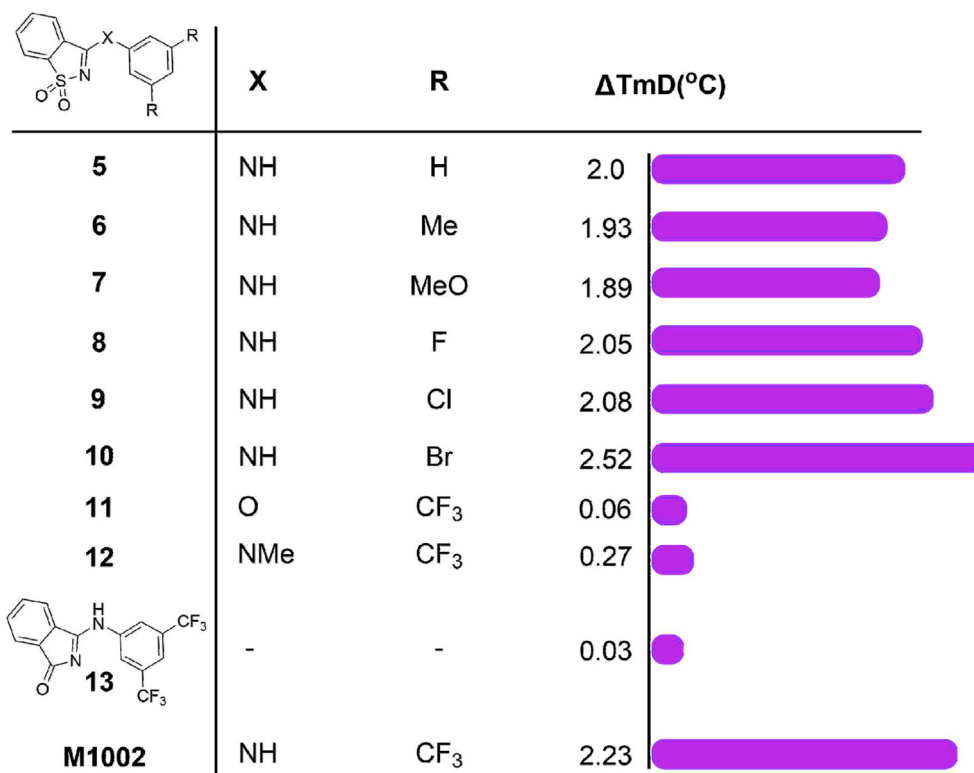


Fig. 7. Activity for M1002 derivatives tested by PTS assay.

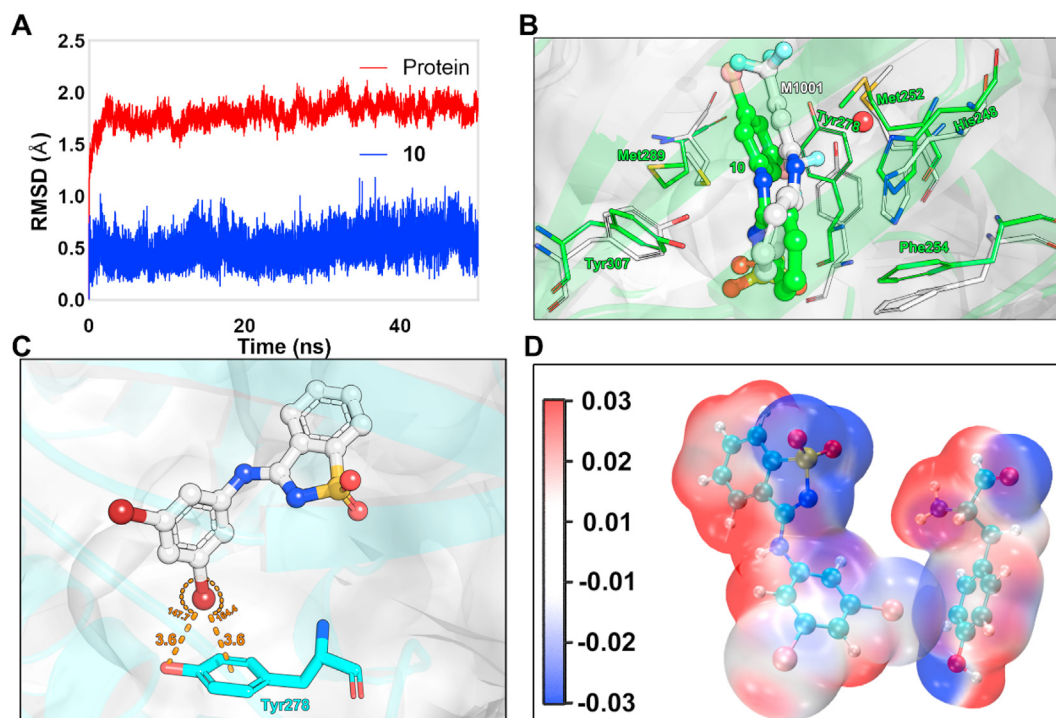


Fig. 8. The docking pose of **10** and potential halogen binding interaction. (A) The ligand and protein RMSD. (B) The superimposition of the **10**-protein complex and the **M1002**-protein complex. The **10**-protein complex is green and the **M1002**-protein complex is white. (C) Potential halogen bond interaction between compound **10** and Tyr278. The white ball-and-stick formula represents **10**, and the cyan one is Tyr278. The distances and angles of the possible halogen bonds between them are shown in orange. (D) The electrostatic potential (ESP) Surfaces of **10** and Tyr278. (For interpretation of the references to color in this figure legend, the reader is referred to the Web version of this article.)

results indicate that **5–10** can activate HIF-2 in a concentration-dependent manner. Compounds **8–10** with electron-withdrawing halogen-substituted B-ring exhibit improved efficacy than **5–7**, which is consistent with our previous simulation and PTS assay results. The only exception is **M1002**. In the PTS assays, **10** showed better binding affinity than **M1002**, but in the luciferase reporter gene assays, 2 μM **M1002** showed better efficacy than 2 μM **10**. It is also worth noting that 20 μM **M1002** seems to be less effective than 2 μM **M1002**, probably due to the cytotoxicity of **M1002** (Fig. 9). To explain these two issues, multiple concentrations of **10** and **M1002** were employed in the luciferase reporter gene assays and cell proliferation assays (Fig. 10).

The results of cell proliferation assays showed that **10** is non-cytotoxic against 786-O-Luc cells at a concentration of 20 μM , while **M1002** significantly inhibits the proliferation of 786-O-Luc cells even at 1 μM (Fig. 10B). The luciferase reporter gene assays indicated that **10** increases the fluorescence of 786-O-HRE-Luc cells by 1.63 times at 20 μM with an EC_{50} of $1.68 \pm 0.62 \mu\text{M}$. The EC_{50} of **M1002** is $0.44 \pm 0.32 \mu\text{M}$. **M1002** at 2.2 μM can increase the fluorescence by 1.41 times, while the fluorescence values of the cell treated with 6.6 μM and 20 μM **M1002** decreased significantly (Fig. 10A). The abnormal results of **M1002** at a high concentration in the luciferase reporter gene assays may be due to its cytotoxicity, which causes a decrease in cell numbers. **M1002** exhibits a lower EC_{50} value than **10**, which is contrary to the binding data in the PTS assays, probably because the trifluoromethyl substituents in **M1002** is beneficial for the cell membrane permeability [35]. Nevertheless, due to the cytotoxicity of **M1002**, **10** still show higher agonistic efficacy at high concentrations. Thus, the cell-based assays could also validate our hypothesis on the agonist binding mode.

Based on the MD simulation results and activity data, we proposed a 2D binding mode of the benisothiazole compound and HIF-2. As shown in Fig. 11, the oxygen atom on the sulfonamide structure of the A-ring can form a hydrogen bond with Tyr307. The replacement of sulfonamides to amides results in loss of activity. Furthermore, the A-ring may form a π - π stack interaction with Phe254. The NH linker can form a hydrogen bond network by bound water with nearby residues His248 and Cys339. The methylation of NH or replacing the nitrogen with oxygen leads to a significant loss of activity, indicating that a hydrogen bond donor is required at this position for HIF-2 binding. Regarding the B-ring, the electron-rich sulfur atoms on Met289 and Met252 can form $n \rightarrow \pi^*$ interactions with the benzene ring of the B-ring. In addition, an electron-donating substituent on the benzene ring, such as CF_3 , is superior for binding compared to an electron-withdrawing one; a

bromo group may form a halogen bond and contribute significantly to the binding with HIF-2.

3. Conclusions

Taken together, we performed MD simulations on the HIF-2 agonist **M1002** in complex with HIF-2 α -PASB domain. Through the calculation of binding free energy and residue energy decomposition, six important amino acid residues that contribute the most to binding were identified. Through hydrogen bond analysis, we suggested a binding mode for these six residues and **M1002**. Subsequently, we synthesized nine **M1002** derivatives and evaluated their activity using protein and cell assay to verify the suggested binding mode. Indeed, compound **10** with bromo-substituted B-ring exhibited better agonistic activity and lower toxicity than **M1002**. The docking results and the ESP calculation results indicate that **10** may form a halogen bond between the bromine atom and Tyr278 of the cavity, thereby enhancing the binding ability. The suggested binding mode of the tested agonists with HIF-2 may provide the basis for future research on more effective HIF-2 agonists.

4. Experimental

4.1. Molecular docking

The structure of the HIF-2-PASB domain was obtained from the PDB database website (PDB ID: 6E3U) and then extracted the 242–360 residues of HIF-2 α from it. Both protein and compounds were prepared by the software Discovery Studio (2020). Residues around 10 Å of the native ligand in the HIF-2 α -PASB domain are defined as binding sites for docking. The CDOCKER protocol of discovery studio (2020) was employed for docking. All settings in the docking were by following per under the default. The conformation with the highest CDOCKER score was used for subsequent dynamic simulation or analysis.

4.2. Molecular dynamics simulation

GROMACS package (version 2019.03) [36] was applied to run conventional MD simulations to investigate the binding mode of **M1002**. The force field amber99sb.ff [20] was employed to parameterize protein. The TIP3P [37] was used for the waters. **M1002** was parameterized using the AnteChamber Python Parser Interface (ACPYE) with amber99sb force field. This **M1002**-protein complex was solvated in an octahedral water box, and then the charge of the system was neutralized by adding 0.150 M chloride and sodium ions. The system was assembled, containing 11,515 water molecules, 37 sodium ions, and 34 chloride ions. First, the steepest descent minimization method was used to minimize the energy of the system by 50,000 steps. In the next step, we restricted the position of heavy atoms to run both NVT equilibration and NPT equilibration by 50,000 steps. The system temperature was maintained at 300 K, and the system pressure was maintained at 1 bar. Upon completion of the two equilibration phases, the system is now well-equilibrated at the desired temperature and pressure. a 500-ns unrestrained simulation was carried out. Every 10 ps, the energy and coordinate system of the trajectory were saved. The hydrogen bond analysis plug-in of Visual Molecular Dynamics (VMD) was applied to analyze the trajectory file [38]. In the simulation trajectory, the bond length changes of the hydrogen bonds formed by **M1002** and the corresponding residues were made into a video using open-source Pymol (version 2.3.0) [39].

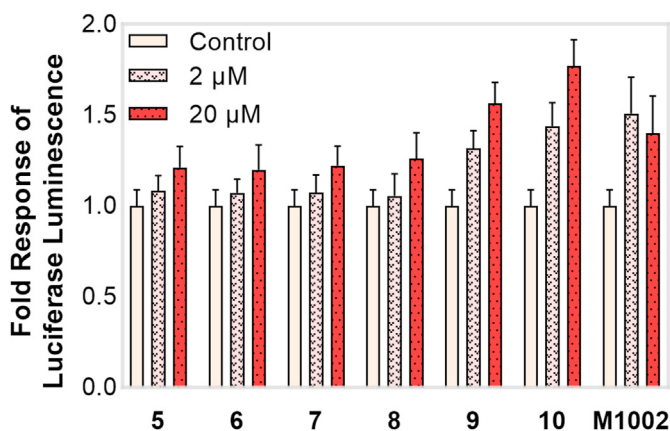


Fig. 9. The agonistic activity of **5–10** evaluated by the HRE luciferase reporter assays. Error bars, mean \pm s.d.; n = 3 (distinct replicates for cell cultures).

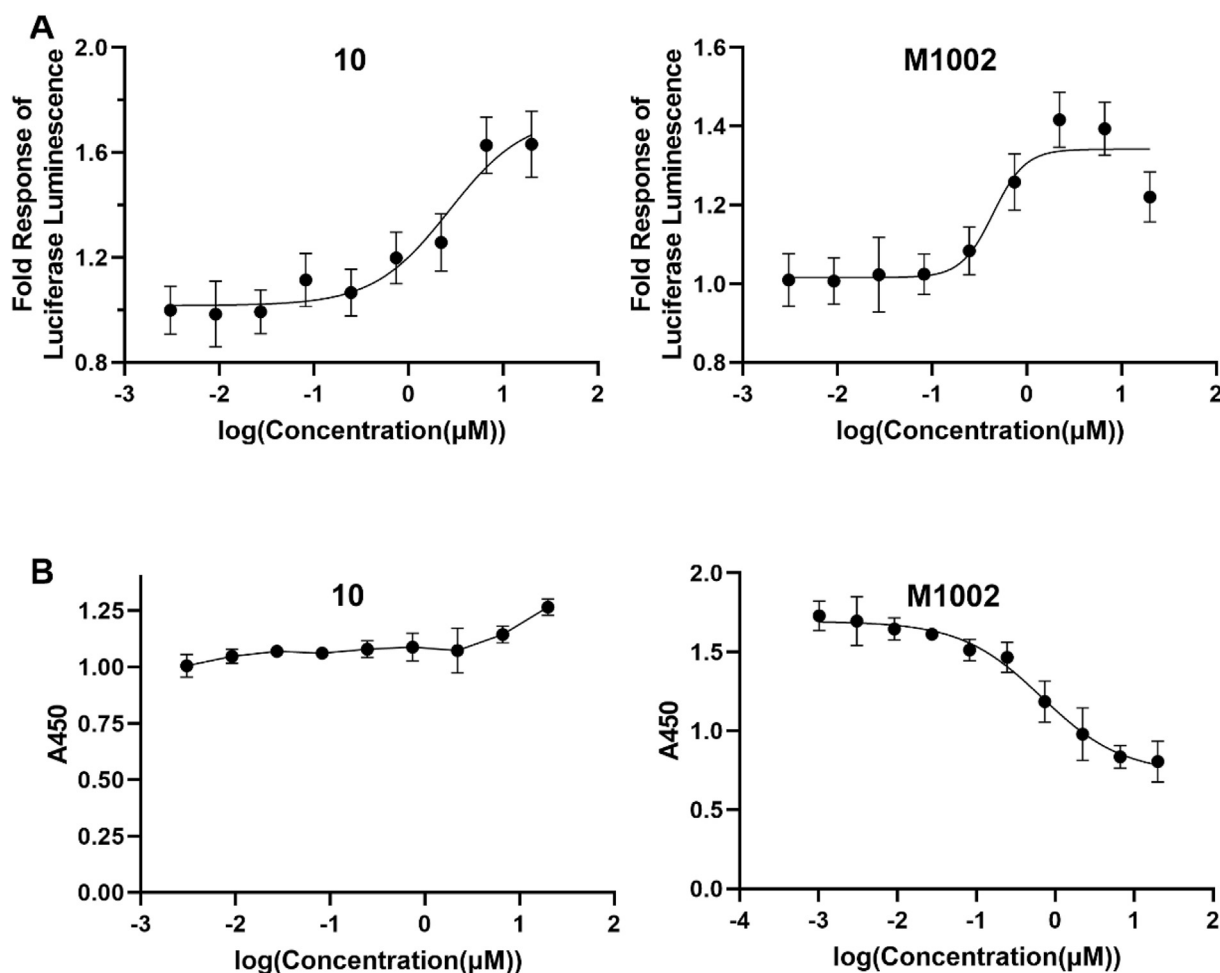


Fig. 10. Biological effect and cytotoxicity of **10** and **M1002**. (A) Results of the luciferase reporter gene for **10** and **M1002**. (B) Cell proliferation assay results of **10** and **M1002** against the 786-O-HRE-Luc cells. Error bars, mean \pm s.d.; n = 3 (distinct replicates for cell cultures).

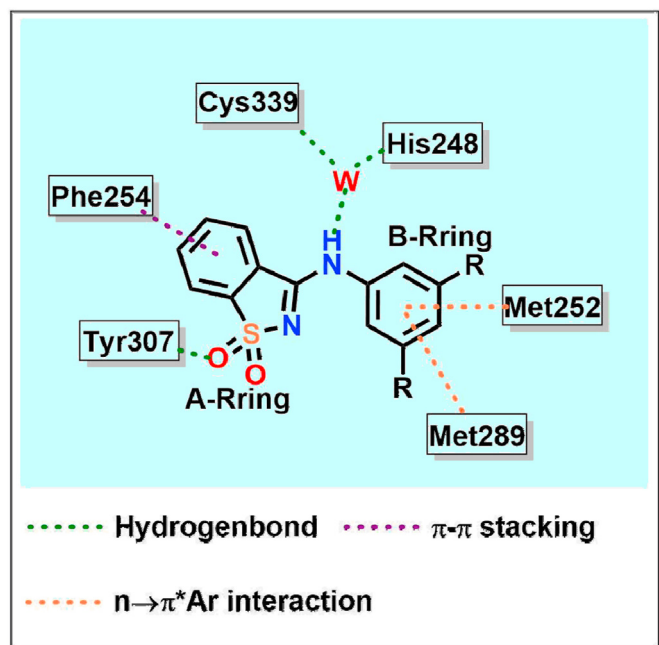


Fig. 11. Schematic diagram of HIF-2 agonist binding mode.

4.3. Free energy calculations and residue decomposition employing the MM-PBSA method

MM-PBSA method has been widely adopted in the estimation of binding free energy in drug research. In our work, the MM-PBSA calculation was performed using the *g_mmpbsa*, a tool of GRO-MACS for MM-PBSA calculations. To understand the binding of protein and ligand at the molecular level, we used *g_mmpbsa* to decompose the free energy of binding to the contribution of each residue to the free energy of binding. We sampled the trajectory every nanosecond to get 500 snapshots. The energy components E_{MM} , G_{polar} , and $G_{nonpolar}$ of the protein-**M1002** complex was calculated for 500 snapshots.

4.4. Chemical synthesis

All chemical reagents and solvents are purchased through commercial sources and used as received. Reactions were monitored using TLC silica gel plates (GF254, 0.25 mm) and visualized under UV light. Hanon MP420 automatic melting point apparatus was used to determine the melting points. The proton nuclear magnetic resonance (1H NMR) and carbon nuclear magnetic resonance (^{13}C NMR) spectra were determined using Bruker AV-300 instruments. EI-mass spectra and high-resolution mass spectra (HRMS) were recorded on a Shimadzu GCMS-2010 mass spectrometer and a Water Q-ToF micro mass spectrometer, respectively.

The purity ($\geq 95\%$) of the target compounds used for biological testing was evaluated by high-performance liquid chromatography (HPLC) analysis, performed on an Amethyst C18–P (4.6×150 mm, $5 \mu\text{M}$, Merck) column eluting with methanol/water (80:20 v:v) at a flow rate of 0.5 mL/min; the peaks were detected at 254 nm under UV. The data collection of a single crystal of **12** was performed on a Bruker Smart Apex2 CCD and Rigaku Saturn CCD diffractometer equipped with graphite monochromated Mo-K α radiation ($\lambda = 0.7107 \text{ \AA}$) at room temperature. The structure was solved with direct methods and refined using OLEX2 and SHELXL-97 programs. The non-hydrogen atoms were located in the successive difference Fourier synthesis. The final refinement was performed by full-matrix least-squares methods with anisotropic thermal parameters for non-hydrogen atoms on F^2 . The hydrogen atoms were added theoretically and riding on the concerning atoms. The parameters used intensity collection and refinements are summarized in Table S1; the selected bond lengths and angles of **12** are summarized in Table S2 and Table S3, respectively.

General Procedure for the Preparation of Compounds M1002(4) – 11. Saccharin (**1a**, 15 g, 0.082 mol) was added to a round bottom flask, and then phosphorus pentachloride (50 g, 0.163 mol) was added. The reaction was heated to 160°C under a nitrogen atmosphere and stirred for 4 h. The reaction mixture was cooled to room temperature and then slowly added into ice water (500 mL). A yellow solid precipitated, and the suspension was filtered. The filter cake was dried to give the crude product **2a** as a yellow solid, which was directly used in the next reaction without further purification. Compound **2a** was added to a round bottom flask, and the corresponding aniline or phenol (the equivalent ratio of **2a** to aniline or phenol: 1 to 1) was added. Dry pyridine (5 mL) was then added to the mixture. The reaction mixture was heated to reflux and stirred for 2–5 h. After the reaction was complete, the solution was cooled to room temperature and poured into water (25 mL). A precipitate precipitated, and the suspension was filtered. The resultant filter cake was purified by chromatography column (hexane: ethyl acetate = 10: 1) to afford the target compounds **4–11**.

4.4.1. 3-((3,5-Bis(trifluoromethyl)phenyl)amino)benzo[d]isothiazole 1,1-dioxide (**M1002, 4**)

White solid. Yield 83.2%. mp $279.2\text{--}279.4^\circ\text{C}$. ^1H NMR (300 MHz, DMSO- d_6) δ 11.26 (s, 1H), 8.58 (s, 2H), 8.42 (d, $J = 7.5$ Hz, 1H), 8.21–8.10 (m, 1H), 7.95 (ddd, $J = 15.1, 9.8, 6.0$ Hz, 3H). HRMS (ESI): calcd. for $\text{C}_{15}\text{H}_8\text{F}_6\text{N}_2\text{O}_2\text{S}$ [$\text{M} + \text{Na}$] $^+$ = 417.0102, found 417.0098. $t_R = 4.993$ min, HPLC purity: 98.71%.

4.4.2. 3-(Phenylamino)benzo[d]isothiazole 1,1-dioxide (**5**)

White solid. Yield 81.8%. mp $> 300^\circ\text{C}$. ^1H NMR (300 MHz, DMSO- d_6) δ 10.86 (s, 1H), 8.49 (d, $J = 7.1$ Hz, 1H), 8.08 (dd, $J = 6.6, 2.0$ Hz, 1H), 7.96–7.80 (m, 4H), 7.54–7.43 (m, 2H), 7.27 (t, $J = 7.4$ Hz, 1H). ^{13}C NMR (75 MHz, DMSO- d_6) δ 157.23, 141.23, 137.98, 134.22, 133.82, 129.53, 128.78, 126.17, 124.07, 122.58, 121.97, 40.83, 40.52, 40.24, 39.99, 39.69, 39.41, 39.13. HRMS (ESI): calcd. for $\text{C}_{13}\text{H}_{10}\text{N}_2\text{O}_2\text{S}$ [$\text{M} + \text{H}$] $^+$ = 259.0536, found 259.0537. $t_R = 3.220$ min, HPLC purity: 99.49%.

4.4.3. 3-((3,5-Dimethylphenyl)amino)benzo[d]isothiazole 1,1-dioxide (**6**)

White solid. Yield 75.2%. mp $> 300^\circ\text{C}$. ^1H NMR (300 MHz, DMSO- d_6) δ 10.77 (s, 1H), 8.55–8.51 (m, 1H), 8.06 (dd, $J = 6.3, 2.3$ Hz, 1H), 7.90 (ddd, $J = 6.5, 4.5, 1.4$ Hz, 2H), 7.51 (d, $J = 1.6$ Hz, 2H), 6.92 (s, 1H), 2.33 (s, 6H). HRMS (ESI): calcd. for $\text{C}_{15}\text{H}_{14}\text{N}_2\text{O}_2\text{S}$ [$\text{M} + \text{H}$] $^+$ = 287.0849, found 287.0849. $t_R = 3.856$ min, HPLC purity: 95.49%.

4.4.4. 3-((3,5-Dimethoxyphenyl)amino)benzo[d]isothiazole 1,1-dioxide (**7**)

White solid. Yield 81.8%. mp $219.0\text{--}219.6^\circ\text{C}$. ^1H NMR (400 MHz, DMSO- d_6) δ 10.72 (s, 1H), 8.48 (d, $J = 7.6$ Hz, 1H), 8.12–8.06 (m, 1H), 7.96–7.85 (m, 2H), 7.12 (d, $J = 2.2$ Hz, 2H), 6.44 (t, $J = 2.2$ Hz, 1H), 3.79 (s, 6H). ^{13}C NMR (75 MHz, DMSO- d_6) δ 161.03, 157.14, 141.02, 139.67, 134.20, 133.80, 128.81, 124.03, 122.00, 100.91, 97.76, 55.84, 40.77, 40.51, 40.24, 39.96, 39.68, 39.40, 39.12. HRMS (ESI): calcd. for $\text{C}_{15}\text{H}_{14}\text{N}_2\text{O}_4\text{S}$ [$\text{M} + \text{H}$] $^+$ = 319.0747, found 319.0751. $t_R = 3.378$ min, HPLC purity: 98.56%.

4.4.5. 3-((3,5-Difluorophenyl)amino)benzo[d]isothiazole 1,1-dioxide (**8**)

White solid. Yield 52.6%. mp $> 300^\circ\text{C}$. ^1H NMR (300 MHz, DMSO- d_6) δ 11.05 (s, 1H), 8.51–8.37 (m, 1H), 8.15–8.06 (m, 1H), 7.99–7.86 (m, 2H), 7.71–7.56 (m, 2H), 7.26–7.11 (m, 1H). HRMS (ESI): calcd. for $\text{C}_{13}\text{H}_8\text{F}_2\text{N}_2\text{O}_2\text{S}$ [$\text{M} + \text{H}$] $^+$ = 295.0347, found 295.0349. $t_R = 3.720$ min, HPLC purity: 99.63%.

4.4.6. 3-((3,5-Dichlorophenyl)amino)benzo[d]isothiazole 1,1-dioxide (**9**)

White solid. Yield 43.1%. mp $> 300^\circ\text{C}$. ^1H NMR (300 MHz, DMSO- d_6) δ 11.03 (s, 1H), 8.49–8.40 (m, 1H), 8.12 (dd, $J = 6.3, 1.9$ Hz, 1H), 8.02–7.86 (m, 4H), 7.54 (t, $J = 1.8$ Hz, 1H). HRMS (ESI): calcd. for $\text{C}_{13}\text{H}_8\text{Cl}_2\text{N}_2\text{O}_2\text{S}$ [$\text{M} + \text{H}$] $^+$ = 326.9756, found 326.9757. $t_R = 5.143$ min, HPLC purity: 97.80%.

4.4.7. 3-((3,5-Dibromophenyl)amino)benzo[d]isothiazole 1,1-dioxide (**10**)

White solid. Yield 60.3%. mp $> 300^\circ\text{C}$. ^1H NMR (300 MHz, DMSO- d_6) δ 10.97 (s, 1H), 8.42 (d, $J = 7.2$ Hz, 1H), 8.13 (d, $J = 13.7$ Hz, 3H), 7.95 (q, $J = 6.6$ Hz, 2H), 7.75 (s, 1H). ^{13}C NMR (75 MHz, DMSO- d_6) δ 157.54, 140.78, 140.66, 134.54, 134.09, 130.51, 128.32, 124.16, 123.70, 122.91, 122.19, 40.81, 40.53, 40.25, 39.98, 39.70, 39.42, 39.14. HRMS (ESI): calcd. for $\text{C}_{13}\text{H}_8\text{Br}_2\text{N}_2\text{O}_2\text{S}$ [$\text{M} + \text{H}$] $^+$ = 414.8746, found 416.8725. $t_R = 5.804$ min, HPLC purity: 99.52%.

4.4.8. 3-(3,5-Bis(trifluoromethyl)phenoxy)benzo[d]isothiazole 1,1-dioxide (**11**)

White solid. Yield 40.2%. mp $92.2\text{--}92.4^\circ\text{C}$. ^1H NMR (300 MHz, DMSO- d_6) δ 8.33–8.29 (m, 1H), 8.24 (dq, $J = 1.6, 0.8$ Hz, 1H), 8.17–8.13 (m, 1H), 8.08 (td, $J = 7.6, 1.5$ Hz, 1H), 8.04–7.98 (m, 1H), 7.92–7.89 (m, 2H). ^{13}C NMR (75 MHz, DMSO- d_6) δ 149.23, 137.17, 136.52, 134.95, 134.87, 133.30, 132.85, 132.40, 131.95, 131.78, 124.66, 122.65, 120.95, 115.43, 111.06, 40.79, 40.51, 40.23, 39.95, 39.68, 39.40, 39.12. HRMS (ESI): calcd. for $\text{C}_{15}\text{H}_7\text{F}_6\text{N}_1\text{O}_3\text{S}$ [$\text{M} + \text{Na}$] $^+$ = 417.9943, found 417.9947. $t_R = 6.092$ min, HPLC purity: 100%.

4.4.9. 3-((3,5-Bis(trifluoromethyl)phenyl)(methyl)amino)benzo[d]isothiazole 1,1-dioxide (**12**)

To a solution of **M1002** (200 mg, 0.5072 mmol, 1.0 eq) in DMF (5 mL) was added potassium carbonate (105.1 mg, 0.7608 mmol, 1.5eq) and then slowly added iodomethane (107.9 mg, 0.7608 mmol, 1.5 eq). After the addition, the reaction was stirred overnight at room temperature. The next day, the reaction was detected by TLC and the reaction was completed. The resulting suspension was quenched by adding water (100 mL). The mixture was extracted with ethyl acetate ($20 \text{ mL} \times 3$) and washed with brine (20 mL). The organic layer was combined and purified with chromatography column (hexane: ethyl acetate = 3: 1) to afford **12**. White solid. Yield 50.2%. mp $223.9\text{--}224.3^\circ\text{C}$. ^1H NMR (300 MHz, DMSO- d_6) δ 8.62–8.55 (m, 2H), 8.41–8.34 (m, 1H), 8.04 (dt, $J = 7.5, 0.9$ Hz, 1H), 7.74 (td, $J = 7.5, 0.8$ Hz, 1H), 7.48 (t, $J = 7.8$ Hz, 1H), 6.11

(s, 1H), 3.65 (s, 3H). ^{13}C NMR (75 MHz, $\text{DMSO}-d_6$) δ 160.28, 144.74, 144.01, 133.64, 133.31, 132.81, 132.36, 130.10, 127.55, 125.80, 125.03, 123.69, 122.54, 121.40, 43.67, 40.79, 40.52, 40.24, 39.96, 39.68, 39.41, 39.13. HRMS (ESI): calcd. for $\text{C}_{16}\text{H}_{10}\text{F}_6\text{N}_2\text{O}_2\text{S}$ $[\text{M} + \text{H}]^+ = 409.0440$, found 409.0442. $t_R = 3.980$ min, HPLC purity: 99.03%. To better understand the structures of these target compounds, the crystal structure of **12** was also determined by X-ray diffraction. As shown in Scheme 1, the crystal structure of **12** was well consistent with the characterization data of NMR and HRMS. The detailed crystal parameters are recorded in the Supplementary data.

4.4.10. 3-((3,5-Bis(trifluoromethyl)phenyl)amino)-1H-isoindol-1-one (**13**)

To a solution of **3a** (1.28 g, 10 mmol, 1.0 eq) in chloroform (20 mL) was added *N,N*-diethylhydroxylamine (1.8 g, 20 mmol, 2 eq) and then heated to reflux for 5 h. Following that, the mixture was quenched with water (50 mL). The resultant mixture was extracted with ethyl acetate (25 mL \times 3) and washed with brine (25 mL). The combined organic layer was dried over anhydrous sodium sulfate, filtrated, and concentrated to afford **4a** (0.7 g, 55%) as a light yellow oil, which was used for the next step without further purification. To a solution of **4a** (0.29 g, 2 mmol, 1.0 eq) in ethanol (5 mL) was added 3,5-bis(trifluoromethyl)aniline (0.5 g, 2.2 mmol, 1.1 eq) and acetic acid (1 mL). The reaction was allowed to be heated to reflux for 5 h. The resultant suspension was quenched with water (20 mL). The mixture was extracted with ethyl acetate (20 mL \times 3) and washed with brine (20 mL). The organic layer was combined and purified with a chromatography column (hexane: ethyl acetate = 20: 1) to afford **13**. White solid. Yield, 34.0%. mp > 300 °C. ^1H NMR (300 MHz, $\text{DMSO}-d_6$) δ 11.10 (s, 1H), 7.83 (t, $J = 47.1$ Hz, 8H). ^{13}C NMR (75 MHz, $\text{DMSO}-d_6$) δ 173.20, 169.78, 150.74, 136.09, 134.22, 133.75, 133.65, 133.51, 133.45, 131.78, 131.35, 123.44, 122.89, 122.60, 117.85, 117.78, 117.73, 117.68, 117.65, 40.78, 40.51, 40.23, 39.95, 39.68, 39.40, 39.12, 25.96. HRMS (ESI): calcd. for $\text{C}_{16}\text{H}_8\text{F}_6\text{N}_2\text{O}$ $[\text{M} + \text{H}]^+ = 359.0614$, found 359.0611. $t_R = 9.687$ min, HPLC purity: 99.49%.

4.5. Protein expression and purification

HIF-2 α -ARNT complex proteins were purified from bacterial lysates by a combination of pre-packed His-Bind resin (Novagen), SP Sepharose (GE Healthcare), and HiLoad 16/60 Superdex 200 pg gel-filtration column (GE Healthcare). The specific protein expression and purification methods were described in refs. 15 and 17 [15,17].

4.6. Protein thermal-shift binding assay

Protein thermal-shift (PTS) assay was conducted in 96-well PCR plates (Thermo Fisher Scientific) using the Protein Thermal Shift Dye Kit (4461146, Thermo Fisher Scientific) on a StepOnePlus qPCR machine (Thermo Fisher Scientific). The experimental method of the instrument was set according to the manufacturer's manual. Each well in the experiment contained 1.5M HIF-2-ARNT protein complex and 10 μM test compound dissolved with DMSO. The buffer used in the experiment contained 20 mM Tris (PH = 8.0) and 400 mM NaCl. The final DMSO concentration in each well was 0.1% [15]. Each compound was tested four times in parallel. The T_m was obtained by calculating the Derivative curve with PTS software 1.3 (Thermo Fisher Scientific). The final ΔT_m value of each compound was obtained by subtracting the blank T_m value.

4.7. Luciferase reporter assay

The 786-O-HRE-Luc single clone cells were obtained by infecting 786-O cells, which were purchased from Cell Bank of Shanghai, Institute of Biochemistry and Cell Biology, Chinese Academy of Sciences with commercial lentivirus (CLS-007L, Qiagen) that delivers a luciferase gene driven by multiple hypoxia response elements (HREs) according to the literature methods [11]. 786-O-HRE-Luc cells were cultured using Roswell Park Memorial Institute (RPMI)-1640 medium (Gibco) and supplemented with 10% FBS (Gibco). For the luciferase reporter gene experiment, the cells were seeded on the 96-well opaque white plate (FCP968, Beyotime) on the first day. After the cells were attached, the corresponding compound DMSO solution was added to each well. Three experiments were performed in parallel for each compound. After 24 h of treatment, One-LumiTM Firefly Luciferase Assay Kit (RG055, Beyotime) was added to each well according to the manufacturer's instructions. The luciferase activity was immediately detected by the multi-function microplate reader (SpectraMax, Molecular Devices). EC_{50} was calculated by using GraphPad Prism 7 software. The graphs are representative results and this experiment was independently repeated three times with similar results.

4.8. Cell proliferation assay

For cell proliferation assay, the 786-O-HRE-Luc cells were seeded on the 96-well plate on the first day. After the cells were attached, the corresponding compound DMSO solution was added to each well to ensure the final concentration (μM) is: 20, 6.67, 2.22, 0.74, 0.25, 0.08, 0.027, 0.009, and 0.003. Three experiments were performed in parallel for each compound. After 24 h of treatment, Cell Counting Kit-8 (C0037, Beyotime) was added to each cell according to the manufacturer's instructions. The 96-well plate was then incubated at 37 °C for 2 h. The absorbance of the samples was detected at 450 nm. The graphs are representative results and this experiment was independently repeated three times with similar results.

4.9. Electrostatic potential calculation

The wavefunctions of compounds **8**, **9**, **10**, and Tyr278 were obtained by Gaussian 09 program [40]. The electrostatic potential (ESP) surfaces were calculated by the "Quantitative analysis of molecular surface" method in the Multiwfn 3.8 program [41]. The color mapped isosurface graphs of ESP and reduced density gradient (RDG) were rendered by VMD 1.9 program [38].

Declaration of competing interest

The authors declare that they have no known competing financial interests or personal relationships that could have appeared to influence the work reported in this paper.

Acknowledgments

This work was supported by grants from the National Natural Science Foundation of China (Grant 81773571), and Jiangsu Province Funds for Excellent Young Scientists (Grant BK20170088). The HIF-2 expression plasmid was generously provided by Professor Dalei Wu (Shangdong University, China).

Appendix A. Supplementary data

Supplementary data to this article can be found online at <https://doi.org/10.1016/j.ejmech.2020.112999>.

References

- [1] F.J. Gonzalez, C. Xie, C. Jiang, The role of hypoxia-inducible factors in metabolic diseases, *Nat. Rev. Endocrinol.* 15 (2018) 21–32.
- [2] T. Hashimoto, F. Shibasaki, Hypoxia-inducible factor as an angiogenic master switch, *Front. Pediatr.* 3 (2015) 33–47.
- [3] F. Melendez-Rodriguez, O. Roche, R. Sanchez-Prieto, J. Aragonés, Hypoxia-inducible factor 2-dependent pathways driving von hippel-lindau-deficient renal cancer, *Front. Oncol.* 8 (2018) 214–221.
- [4] H. Tian, S.L. McKnight, D.W.J.G. Russell, development, Endothelial PAS domain protein 1 (EPAS1), a transcription factor selectively expressed in endothelial cells, *Genes Dev.* 11 (1997) 72–82.
- [5] P.J. Erbel, P.B. Card, O. Karakuzu, R.K. Bruick, K.H. Gardner, Structural basis for PAS domain heterodimerization in the basic helix–loop–helix-PAS transcription factor hypoxia-inducible factor, *Proc. Natl. Acad. Sci. U. S. A.* 100 (2003) 15504–15509.
- [6] L. Schito, G.L. Semenza, Hypoxia-inducible factors: master regulators of cancer progression, *Trends Cancer* 2 (2016) 758–770.
- [7] M.J. Koury, V.H. Haase, Anaemia in kidney disease: harnessing hypoxia responses for therapy, *Nat. Rev. Neurol.* 11 (2015) 394–410.
- [8] Y. Yu, Q. Yu, X. Zhang, Allosteric inhibition of HIF-2 α as a novel therapy for clear cell renal cell carcinoma, *Drug Discov. Today* 24 (2019) 2332–2340.
- [9] E.M. Wallace, J.P. Rizzi, G. Han, P.M. Wehn, Z. Cao, X. Du, T. Cheng, R.M. Czerwinski, D.D. Dixon, B.S. Goggins, J.A. Grina, M.M. Halfmann, M.A. Maddie, S.R. Olive, S.T. Schlachter, H. Tan, B. Wang, K. Wang, S. Xie, R. Xu, H. Yang, J.A. Josey, A small-molecule antagonist of hif2 α is efficacious in preclinical models of renal cell carcinoma, *Canc. Res.* 76 (2016) 5491–5500.
- [10] N. Gupta, J.B. Wish, Hypoxia-inducible factor prolyl hydroxylase inhibitors: a potential new treatment for anemia in patients with CKD, *Am. J. Kidney Dis.* 69 (2017) 815–826.
- [11] P.M. Wehn, J.P. Rizzi, D.D. Dixon, J. Grina, S.T. Schlachter, B. Wang, R. Xu, H. Yang, X. Du, G. Han, K. Wang, Z. Cao, T. Cheng, R.M. Czerwinski, B.S. Goggins, H. Huang, M.M. Halfmann, M.A. Maddie, E.L. Morton, S.R. Olive, H. Tan, S. Xie, T. Wong, J.A. Josey, E.M. Wallace, Design and activity of specific hypoxia-inducible factor 2 α (HIF-2 α) inhibitors for the treatment of clear cell renal cell carcinoma: discovery of clinical candidate (S)-3-((2,2-difluoro-1-hydroxy-7-(methylsulfonyl)-2,3-dihydro-1H-inden-4-yl)oxy)-5-fluorobenzonitrile (PT2385), *J. Med. Chem.* 61 (2018) 9691–9721.
- [12] T.H. Scheuermann, D.R. Tomchick, M. Machius, Y. Guo, R.K. Bruick, K.H. Gardner, Artificial ligand binding within the HIF2 PAS-B domain of the HIF2 transcription factor, *Proc. Natl. Acad. Sci. U. S. A.* 106 (2009) 450–455.
- [13] R. Xu, K. Wang, J.P. Rizzi, H. Huang, J.A. Grina, S.T. Schlachter, B. Wang, P.M. Wehn, H. Yang, D.D. Dixon, R.M. Czerwinski, X. Du, E.L. Ged, G. Han, H. Tan, T. Wong, S. Xie, J.A. Josey, E.M. Wallace, 3-[(1S,2S,3R)-2,3-Difluoro-1-hydroxy-7-methylsulfonyl-indan-4-yl]oxy-5-fluoro-benzonitrile (PT2977), a hypoxia-inducible factor 2 α (HIF-2 α) inhibitor for the treatment of clear cell renal cell carcinoma, *J. Med. Chem.* 62 (2019) 6876–6893.
- [14] E. Jonasch, E.K. Park, S. Thamake, M. Hirmand, W.M. Linehan, R. Srinivasan, An open-label phase II study to evaluate PT2977 for the treatment of von Hippel-Lindau disease-associated renal cell carcinoma, *J. Clin. Oncol.* 37 (2019). TPS680–TPS680.
- [15] D. Wu, X. Su, J. Lu, S. Li, B.L. Hood, S. Vasile, N. Potluri, X. Diao, Y. Kim, S. Khorasanizadeh, F. Rastinejad, Bidirectional modulation of HIF-2 activity through chemical ligands, *Nat. Chem. Biol.* 15 (2019) 367–376.
- [16] A.S. Chong, P.C. Anderson, Molecular dynamics simulations of the hypoxia-inducible factor pas-b domain confirm that internally bound water molecules function to stabilize the protein core for ligand binding, *Biochemistry* 59 (2020) 450–459.
- [17] D. Wu, N. Potluri, J. Lu, Y. Kim, F. Rastinejad, Structural integration in hypoxia-inducible factors, *Nature* 524 (2015) 303–308.
- [18] F. Correa, J. Key, B. Kuhlman, K.H. Gardner, Computational repacking of HIF-2 α cavity replaces water-based stabilized core, *Structure* 24 (2016) 1918–1927.
- [19] G. Wu, D.H. Robertson, C.L. Brooks Iii, M. Vieth, Detailed analysis of grid-based molecular docking: a case study of CDOCK—A CHARMM-based MD docking algorithm, *J. Comput. Chem.* 24 (2003) 1549–1562.
- [20] V. Hornak, R. Abel, A. Okur, B. Strockbine, A. Roitberg, C. Simmerling, Comparison of multiple Amber force fields and development of improved protein backbone parameters, *Proteins* 65 (2006) 712–725.
- [21] R. Kumari, R. Kumar, C. Open, Source Drug Discovery, A. Lynn, g_mmpbsa—a GROMACS tool for high-throughput MM-PBSA calculations, *J. Chem. Inf. Model.* 54 (7) (2014) 1951–1962.
- [22] S. Grimme, Do special noncovalent π – π stacking interactions really exist? *Angew. Chem., Int. Ed. Engl.* 47 (2008) 3430–3434.
- [23] T.P. Tauer, M.E. Derrick, C.D. Sherrill, Estimates of the ab initio limit for sulfur– π interactions: the H₂S–benzene dimer, *J. Phys. Chem.* 109 (2005) 191–196.
- [24] C.Q. Wan, J. Han, T.C.W. Mak, Intermolecular S \cdots π interactions in crystalline sulfanyl-triazine derivatives, *New J. Chem.* 33 (2009) 707–712.
- [25] S.K. Singh, A. Das, The n \rightarrow π^* interaction: a rapidly emerging non-covalent interaction, *Phys. Chem. Chem. Phys.* 17 (2015) 9596–9612.
- [26] M.S. Elsayed, M.E. El-Araby, R.T. Serya, K.A. Abouzid, Virtual screening and synthesis of new chemical scaffolds as VEGFR-2 kinase inhibitors, *Arzneimittelforschung* 62 (2012) 554–560.
- [27] K.V. Luzyanin, V.Y. Kukushkin, M.N. Kopylovich, A.A. Nazarov, M. Galanski, A.J.L. Pombeiro, Novel and mild route to phthalocyanines and 3-iminoisoindolin-1-one via n,n-diethylhydroxylamine-promoted conversion of phthalonitriles and a dramatic solvent-dependence of the reaction, *Adv. Synth. Catal.* 350 (2008) 135–142.
- [28] Z.Q. Zhang, S. Uth, D.J. Sandman, B.M. Foxman, Structure, polymorphism and thermal properties of phenyliminoisoindolines, *J. Phys. Org. Chem.* 17 (2004) 769–776.
- [29] K. Huynh, C.L. Partch, Analysis of protein stability and ligand interactions by thermal shift assay, *Curr. Protein Pept. Sci.* 79 (2015), 28.9.1–28.9.14.
- [30] N.K. Shinada, A.G. de Brevern, P. Schmidtke, Halogens in protein-ligand binding mechanism: a structural perspective, *J. Med. Chem.* 62 (2019) 9341–9356.
- [31] E. Margiotta, S.C.C. van der Lubbe, L. de Azevedo Santos, G. Paragi, S. Moro, F.M. Bickelhaupt, C. Fonseca Guerra, Halogen bonds in ligand–protein systems: molecular orbital theory for drug design, *J. Chem. Inf. Model.* 60 (2020) 1317–1328.
- [32] J.S. Murray, P. Politzer, The electrostatic potential: an overview, *Wiley Interdiscip. Rev. Comput. Mol. Sci.* 1 (2011) 153–163.
- [33] Y.L. Lin, A. Aleksandrov, T. Simonson, B. Roux, An overview of electrostatic free energy computations for solutions and proteins, *J. Chem. Theor. Comput.* 10 (2014) 2690–2709.
- [34] H. Wang, W. Wang, W.J. Jin, σ -hole bond vs π -hole bond: a comparison based on halogen bond, *Chem. Rev.* 116 (2016) 5072–5104.
- [35] M. Bassetto, S. Ferla, F. Pertusati, Polyfluorinated groups in medicinal chemistry, *Future Med. Chem.* 7 (2015) 527–546.
- [36] M.J. Abraham, T. Murtola, R. Schulz, S. Pall, J.C. Smith, B. Hess, E.J.S. Lindahl, GROMACS: high performance molecular simulations through multi-level parallelism from laptops to supercomputers, *SoftwareX* 1 (2015) 19–25.
- [37] W.L. Jorgensen, J. Chandrasekhar, J.D. Madura, R.W. Impey, M.L. Klein, Comparison of simple potential functions for simulating liquid water, *J. Chem. Phys.* 79 (1983) 926–935.
- [38] W. Humphrey, A. Dalke, K. Schulten, VMD: visual molecular dynamics, *J. Mol. Graph.* 14 (1996) 33–38.
- [39] W.L. DeLano, PyMOL: an open-source molecular graphics tool, *CCP4 Newsletter on Protein Crystallography* 40 (2002) 82–92.
- [40] Gaussian 09, Revision A.02 M.J. Frisch, G.W. Trucks, H.B. Schlegel, G.E. Scuseria, M.A. Robb, J.R. Cheeseman, G. Scalmani, V. Barone, G.A. Petersson, H. Nakatsuji, X. Li, M. Caricato, A. Marenich, J. Bloino, B.G. Janesko, R. Gomperts, B. Mennucci, H.P. Hratchian, J.V. Ortiz, A.F. Izmaylov, J.L. Sonnenberg, D. Williams-Young, F. Ding, F. Lipparini, F. Egidi, J. Goings, B. Peng, A. Petrone, T. Henderson, D. Ranasinghe, V.G. Zakrzewski, J. Gao, N. Rega, G. Zheng, W. Liang, M. Hada, M. Ehara, K. Toyota, R. Fukuda, J. Hasegawa, M. Ishida, T. Nakajima, Y. Honda, O. Kitao, H. Nakai, T. Vreven, K. Throssell, J.A. Montgomery Jr., J.E. Peralta, F. Ogliaro, M. Bearpark, J.J. Heyd, E. Brothers, K.N. Kudin, V.N. Staroverov, T. Keith, R. Kobayashi, J. Normand, K. Raghavachari, A. Rendell, J.C. Burant, S.S. Iyengar, J. Tomasi, M. Cossi, J.M. Millam, M. Klene, C. Adamo, R. Cammi, J.W. Ochterski, R.L. Martin, K. Morokuma, O. Farkas, J.B. Foresman, D.J. Fox, Gaussian, Inc., Wallingford CT (2016).
- [41] T. Lu, F. Chen, Multiwfn: a multifunctional wavefunction analyzer, *J. Comput. Chem.* 33 (2012) 580–592.